

The use of the Rietveld method and pairs distribution function analysis to study the pressure dependence of the trigonal SnSe₂ and SnS₂ structure

J. C. de Lima^{1,a)}, Z. V. Borges¹, C. M. Poffo², S. M. Souza³, D. M. Trichês³, and R.S. de Biasi⁴

¹Departamento de Engenharia Mecânica, Universidade Federal de Santa Catarina, Programa de Pós-Graduação em Ciência e Engenharia de Materiais, Campus Universitário Trindade, C.P. 476, 88040-900 Florianópolis, Santa Catarina, Brazil

²Universidade Federal de Santa Catarina, Campus de Araranguá, 88900-000 Araranguá, Santa Catarina, Brazil.

³Departamento de Física, Instituto de Ciências Exatas, Universidade Federal do Amazonas, 69077-000 Manaus, Amazonas, Brazil

⁴Seção de Engenharia Mecânica e de Materiais, Instituto Militar de Engenharia, 22290-270 Rio de Janeiro, RJ, Brazil

ABSTRACT

A nanostructured trigonal SnSe₂ was produced by mechanical alloying, and the effect of high-pressures up to 25.8 GPa on it was investigated. The literature reports refined structural data for SnS₂ for pressures up to 20 GPa. These data were used as input data in a crystallographic software to calculate the shell structures around the Sn, Se, and S atoms placed at the origin. The shell structures were used to simulate the partial and total structure factors $S_{i-j}(K)$ and $S(K)$, and by Fourier transformation the partial and total pairs distribution functions $G_{i-j}(R)$ and $G(R)$ were obtained. The effect of high-pressure on the SnSe₂ and SnS₂ structures were followed by observing the changes in the $G_{i-j}(R)$ functions. Also, the effect of high-pressure on the smallest angle Sn-X (X=Se,S)-Sn, intralayer distance Sn-X (X=Se,S),

and interlayers distance X-X (X=Se,S) was studied. The interlayers distance X-X (X=Se,S) changes faster than the intralayer distance Sn-X (X=Se,S). An enhancement of the average power factor at 20 GPa and 800 K for SnS₂ was reported. Using the interlayers distance S-S and intralayer distance Sn-S, it was evidenced that the enhancement of average power factor may be associated with the changes of the interlayers distance S-S that is faster than that of the intralayer distance Sn-S.

Keywords: High pressure; X-ray diffraction; Rietveld Method; Pairs Distribution Function; Thermoelectric layered compound

a) Author to whom correspondence should be addressed. Electronic mail: joao.cardoso.lima@ufsc.br or jcardoso.delima@gmail.com

I. Introduction

Despite the extraordinary progress in the development of DACs, allowing that several dozen GPa be achieved, they have yet a limited window of few tens (two or three) of degrees, imposing a restriction in the angular range (2θ) in which the X-ray diffraction (XRD) patterns are measured. This limitation makes difficult to visualize the effect of high-pressure on the structure being studied, as well as it increases the difficulties in the determination of new high-pressure structure phases emerging due to the few number of diffraction peaks recorded.

Trying to overcome the difficulties mentioned above, at least partially, we implemented an approach combining the Rietveld method (RM) [1] and pairs distribution

function (PDF) analysis [2–4]. The details of this approach are described in Refs. [5,6,7], and it will not be repeated here. RM has been implemented in several computational packages, such as the GSAS package [8], which has been employed to refine and/or to determine structures of the crystallographic phases of single crystal and polycrystalline solids. The theoretical description of PDF analysis as well as its applications to the liquid and amorphous materials is well documented in the literature [2–4] and will not be repeated here. The approach to be presented in this study requires only the knowledge of the structure of the crystalline material. It has already been used by us to investigate the effect of moderate (MPa) and high (GPa) pressures on nanocrystalline materials [6,7]. In order to corroborate the validity of this approach and also make it more explicit for readers, it was also applied to the Ta₂O₅ orthorhombic compound previously studied using XRD, RM, and PDF [9,10]. The results obtained using this approach were compared with those reported in Refs. [9,10], and an excellent agreement was observed.

The isostructural SnSe₂ and SnS₂ compounds (space group P-3 m 1, 164) and based on SnS₂-, SnSe₂-alloys have great potential for applications in thermoelectric (TE) devices like solid-state coolers or generators at moderate and high temperatures [9]. Recently, our group produced using the mechanical alloying (MA) technique the SnSe₂ compound, in the nanostructured form.

The effect of high-pressure up to 25.8 GPa on SnSe₂ was investigated using X-ray diffraction (XRD) measurements and synchrotron radiation. The recorded XRD patterns were refined using RM. The refined structural data are used as “input data” in a crystallographic software such as Crystal Office 98® from the Atomic Softtek - Canada, and using the option (tool “output + coordinates + shell structure”) the shell structure around a specific atom *i* placed at the origin is obtained. Recently, Filsø *et al.* [11], using single crystal

XRD measurements and DFT calculations, investigated the effect of high-pressure up to 20 GPa on the SnS₂ compound. The recorded XRD patterns were refined using RM.

Javed *et al.* [12], using first principles calculations, studied along *a*- and *c*-axes, the thermoelectric power (*S*), conductivity electrical (σ), and power factor (PF) properties for atmospheric, 10 and 20 GPa, at temperatures 300 K, 500 K and 800 K. Those researchers reported an enhancement in average PF at 20 GPa and 800 K, leading to values of figure of merit *ZT* between 1 – 2.5. TE materials are characterized for technological applications by the dimensionless figure of merit *ZT*. To our best knowledge, similar study was not found in the literature for SnSe₂.

As mentioned previously, the approach combining the Rietveld method and pairs distribution function analysis requires only the knowledge of the structure of the crystalline material to build the partial pairs distribution functions (PPDFs) as well as the total pairs distribution function (PDF). The PDF functions can give a more accurate insight structure of the effect of high-pressure. We are using the refined structural data for SnSe₂ to calculate the shell structures around Sn and Se atoms placed at the origin and those reported for SnS₂ to calculate the shell structures around Sn and S atoms. Thus, the main goal of this study is to compare the PPDFs and PDFs for the SnS₂ and SnSe₂ compounds. In addition, it will be tried to associate, at least partially, the structural changes promoted by high-pressure on SnS₂ with the changes observed in the macroscopic physical thermoelectric power (*S*), conductivity electrical (σ), and power factor (PF) properties.

II. Experimental procedure

The nanostructured SnSe₂ powder used in this study was the same used in a previous study [13]. Then, details involving its production are described in [13] and will not be

repeated here. *In-situ* XRD patterns were recorded for pressures listed in Table 1, at atmospheric pressure, at the X-ray Diffraction and Spectroscopy (XDS) station of the LNLS synchrotron radiation facility (Brazil). The XDS station consists of a nitrogen-cooled Si (311) double-crystal monochromator to select the incoming energy and a Dectris Pilatus 300 K image plate detector to record the diffracted beam. The present experiment was performed using a wavelength of $\lambda = 0.61990 \text{ \AA}$ (20.0 keV). The sample was loaded in a stainless-steel gasket hole of 150 μm diameter. The diamond culet was 350 μm in diameter and the thickness of the gasket after indentation was 65 μm . As the pressure-transmitting medium, a methanol-ethanol (4:1) solution was used, which is hydrostatic in the 0–10 GPa pressure range and nonhydrostatic for larger pressures. A Membrane Diamond Anvil Cell (MDAC) with an opening of 22.0° (2θ) was used. The sample-to-detector distance (292 mm) and instrumental broadening were determined from diffraction data of standard crystalline LaB_6 powder. The pressure was determined by the fluorescence shift of a ruby micropiece [14] loaded in the sample chamber. An exposure time of 10 min was used for all measurements. The two-dimensional diffraction patterns were converted to intensity versus 2θ data using the FIT2D software [15]. All the XRD patterns were refined using the Rietveld method [1] implemented in the computational GSAS package [8]. For SnS_2 , all the experimental details about the preparation of sample, XRD measurements, pressure applied, and data refinement are described in Ref. [11], and they will not be repeated here.

III. The use of the structural data for SnSe_2 and SnS_2 to build the shell structure

At room temperature and atmospheric pressure, the isostructural SnS_2 and SnSe_2 compounds crystallize in a trigonal structure (space group P-3 m 1, No. 164), with the Sn

atoms occupying the Wyckoff position $1a$ (0,0,0) and S, Se atoms occupying the position $2d$ ($1/3, 2/3, Z$) [16]. Figure 1 shows the conventional unit cell for $\text{Sn}(\text{S},\text{Se})_2$. These compounds are characterized by intralayer covalent Sn–Se, Sn–S bonds and interlayer $\text{Se}\cdots\text{Se}$, $\text{S}\cdots\text{S}$ of the van der Waals type. As previously mentioned, the effect of high-pressure on SnSe_2 for pressures up to 25.8 GPa was studied using XRD measurements, and the recorded patterns were refined using RM [1] implemented in the GSAS package [8]. Table 1 lists the refined lattice parameters and the Z -coordinate for the Se atoms at position $2d$ ($1/3, 2/3, Z$). For SnS_2 , these structural data were taken from the paper by Filsø *et al.*[11], and they are listed in Table 2.

The space group P-3 m 1 (164), lattice parameters for SnSe_2 (Table 1) and for SnS_2 (Table 2), Wickoff positions $1a$ (0,0,0) for the Sn atoms and $2d$ ($1/3,2/3,Z$) for the Se, S atoms were used as “input data” for the Crystal Office software® [17], and using the software’s tools “*Output + Coordinates + Shell Structure*” the shell structures around Sn and Se atoms placed at the origin for SnSe_2 , and around Sn and S atoms placed at the origin for SnS_2 were calculated up to $R_{max} = 25 \text{ \AA}$ (arbitrarily chosen). The shell structures give the coordination numbers N_{i-j} and interatomic distances R_{i-j} with respect to the atom i placed at the origin, i.e., $N_{\text{Sn-Sn}}, R_{\text{Sn-Sn}}, N_{\text{Sn-Se}}, R_{\text{Sn-Se}}, N_{\text{Se-Se}}, R_{\text{Se-Se}}$ for SnSe_2 , and $N_{\text{Sn-Sn}}, R_{\text{Sn-Sn}}, N_{\text{Sn-S}}, R_{\text{Sn-S}},$ and $N_{\text{S-S}}, R_{\text{S-S}}$ for SnS_2 . The shell structures were used as “input data” for a computational FORTRAN code describing the expression (1) of Ref. [5] to simulate the partial structure factors $S_{i-j}(K)$, i.e., $S_{\text{Sn-Sn}}(K), S_{\text{Sn-Se}}(K), S_{\text{Se-Se}}(K)$ for SnSe_2 , and $S_{\text{Sn-Sn}}(K), S_{\text{Sn-S}}(K), S_{\text{S-S}}(K)$ for SnS_2 , using a value $K_{max} = 30 \text{ \AA}^{-1}$ arbitrarily chosen. By Fourier transformation of the simulated $S_{i-j}(K)$ factors, the partial and total reduced total distribution functions $\gamma_{i-j}(R)$ and $\gamma(R)$, the partial and total pairs distribution functions $G_{i-j}(R)$ and $G(R)$, and partial and total radial distribution functions $RDF_{i-j}(R)$ and $RDF(R)$ were obtained. To build the total $S_{\text{SnSe}_2}(K)$

and $S_{SnS_2}(K)$ factors, the weights $W_{Sn-Sn}(K)$, $W_{Sn-Se}(K)$, $W_{Se-Se}(K)$, $W_{Sn-S}(K)$ and $W_{S-S}(K)$ were computed. All the computational FORTRAN codes describing the expressions given in Section II of Ref. [5] were written by one of the authors (J.C. de Lima).

IV. Results and discussion

Figures 2(a)-(b) show the $\gamma_{SnSe_2}(R)$ functions obtained by Fourier transformation of the simulated $S_{SnSe_2}(K)$ factors, at ambient conditions ($T = 300$ K, $P = 0$ GPa), with different values of K_{max} . In this figure is also shown the experimental $\gamma_{SnSe_2}(R)$ function (green curve in Fig. 2(a)) obtained by Fourier transformation of the experimental $S_{SnSe_2}(K)$ factor derived from the XRD data recorded at ambient conditions with the SnSe₂ powder within the DACs. In order to reproduce the angular range reached using a DAC, a conventional source (Cu and Mo target), and a synchrotron source, the values of K_{max} 5, 8, 16, 30 and 60 Å⁻¹, with a step $\Delta K = 0.025$ Å⁻¹, were considered to obtain the $S_{i-j}(K)$ factors. For simulations, the lattice parameters for pressure $P = 0$ GPa listed in Table 1 were considered. Based on Ref. [5], the value of K_{max} 30 Å⁻¹ was assumed in this study. The resolution of $\gamma(R)$ function is given by $\Delta R = 3.8/K_{max}$ [3], and for K_{max} 30 Å⁻¹, $\Delta R = 0.127$ Å. From these figures one can see that the approach combining RM and PDF analysis can give a insight structure of the effect of high-pressure, as shown in Fig. 2(b). However, accurate high-pressure XRD measurements and accurate determination of the structure are necessary.

Figures 3(a)-(c), (d)-(f), and (g)-(i) show the $G_{Sn-Sn}(R)$, $G_{Sn-Se}(R)+G_{Sn-S}(R)$, and $G_{Se-Se}(R)+G_{S-S}(R)$ functions for SnSe₂ and SnS₂, respectively, obtained by Fourier transformation of their respective simulated $S_{i-j}(K)$ with the value of K_{max} 30 Å⁻¹. According to the calculated shell structures for SnSe₂, the first coordination shells of the $G_{Sn-Sn}(R)$, $G_{Sn-Se}(R)$, and G_{Se-

$_{Se}(R)$ functions are formed by 6 Sn-Sn pairs at 3.811 Å, 6 Sn-Se pairs at 2.682 Å, and two subshells each one containing 6 Se-Se pairs at 3.776 Å and 3.881 Å, respectively. For SnS₂, at ambient conditions, the first coordination shells of the $G_{Sn-Sn}(R)$, $G_{Sn-S}(R)$, and $G_{S-S}(R)$ functions are formed by 6 Sn-Sn pairs at 3.646 Å, 6 Sn-S pairs at 2.560 Å, and two subshells containing 3 S-S pairs at 3.595 Å and 9 S-S pairs at 3.646 Å, respectively. With increasing pressure, the effect of pressure on $G_{Sn-Sn}(R)$ of SnSe₂ and SnS₂ is only visible for the coordination shell located between $\approx 6.3 \text{ \AA} < R < \approx 7.3 \text{ \AA}$, where the two subshells tend to overlap; On $G_{Sn-Se}(R)$ and $G_{Sn-S}(R)$ of SnSe₂ and SnS₂, with exception of the first coordination shell, the effect is to overlap the subshells forming the coordination shells. This effect seems to be more significant for SnSe₂; and on $G_{Se-Se}(R)$ and $G_{S-S}(R)$ of SnSe₂ and SnS₂, the effect is to split the two subshells forming the first coordination shell. This effect seems to be more significant for SnS₂. Simulated total $G_{SnSe_2}(R)$ and $G_{SnS_2}(R)$ for the pressures used are shown in Fig. 4(a)-(c). With increasing pressure, no splitting is observed for the first coordination shell of SnSe₂ and SnS₂; The second coordination shell of SnSe₂ is splitted into two subshells partially overlapped, while that of SnS₂, no splitting is observed.

Figure 5 shows the pressure dependence of the smallest angle Sn-X(X=Se,S)-Sn, intralayer interatomic distances Sn-X(X=Se,S), and interlayers interatomic distances X-X (X=Se,S). From this figure, one can see that, with increasing pressure, the value of the smallest angle Sn-Se-Sn increase for the pressures up to ≈ 18 GPa, decreasing slightly for larger pressures, while the smallest angle Sn-S-Sn decreases for the pressures used. With respect to the intralayer distances Sn-Se and Sn-S, with increasing pressure, they decrease for the pressures used. However, the later decreases faster. For the distance Sn-S, the increase between 12 and 14 GPa can be associated to the nonhydrostaticity of the pressure transmitting

médium. With respect to the interlayers distance X-X (X=Se,S), with increasing pressure, they decrease continuously. For SnS₂, it decreases faster.

As previously mentioned, Javed *et al.* [12], using a first principles calculations, studied for SnS₂ the macroscopic thermoelectric power (S), conductivity electrical (σ), power factor (PF) properties along the *a*- and *c*-axes, and average PF at atmospheric pressure (P = 0 GPa), 10 GPa and 20 GPa and at temperatures 300 K, 500 K and 800 K. Their results are shown in Fig. 6(a)-(d). Thus, it is interesting to try to correlate the effect of high-pressure previously shown with the macroscopic thermoelectric properties of SnS₂. The performance of TE material is characterized by its dimensionless figure of merit $ZT = (S^2\sigma)T/k$, where S is the thermoelectric power, σ the electrical conductivity, k the thermal conductivity, and T the absolute temperature. The $S^2\sigma$ is named the power factor (PF). For technological TE applications, $ZT > 1$ is desired. Those researchers reported an enhancement of TE performance of SnS₂ at 20 GPa and 800 K ($1 < ZT < 2.5$). From the Fig. 6(a), one can see that, with increasing pressure, carrier concentration and temperature, the thermoelectric power S decreases. At atmospheric pressure and 800 K, the value of S along *a*-axis is larger than the value along *c*-axis. At 10 GPa and 800 K, the value of S along *a*-axis is slightly larger than the value along *c*-axis, and at 20 GPa and 800 K, the values of S along *a*- and *c*-axes are similar. From the Fig. 6(b), one can see that, with increasing pressure, carrier concentration and temperature, the electrical conductivity σ increases. At atmospheric pressure and 800 K, the value of σ along *a*-axis is larger than the value along *c*-axis. At 10 GPa and 800 K, the values of σ along *a*- and *c*-axes are similar, and at 20 GPa and 800 K, the value of σ along *c*-axis is larger than the value of σ along *a*-axis. This behavior at 20 GPa and 800 K may be associated with the interlayers distance S-S that decreases faster than the Sn-S one, suggesting that the electronic repulsion begins to play an important role. From the

Fig. 6(c), one can see that the power factor (PF) increases with increasing the carrier concentration and temperature, but it can decrease with increasing pressure. At atmospheric pressure and 800 K, the value of PF along *a*-axis is larger than the value of PF along *c*-axis. This behavior seems to be in accordance with the values of *S* and σ along this axis. At 10 GPa and 800 K, value of PF along the *a*-axis is even larger than the value along *c*-axis, but the difference between them decreased, and at 20 GPa and 800 K, value of PF along the *c*-axis is larger than the value along *a*-axis. This behavior seems to be in accordance with the values of *S* and σ along this axis. Thus, the increase in PF along the *c*-axis may be associated with the interlayers distance S-S that decreases faster than the Sn-S one, suggesting that the electronic repulsion begins to play an important role, mainly, in the electrical conductivity.

From the Fig. 6(d), one can see that the average power factor (PF) increases with increasing pressure and carrier concentration. At 20 GPa and 800 K, the increase in average PF may be associated to the increase in value of the electrical conductivity along *c*-axis due to the fast decrease in the interlayers distance S-S, as discussed early. To our best knowledge, there are no similar data for SnSe₂ in the literature, and therefore, similar analysis is inaccurate. From Fig. 5, one can see that, with increasing pressure, both the intralayer distance Sn-Se (d_{intra}) and interlayers interatomic distance Se-Se (d_{inter}) decrease continuously for SnSe₂, while for SnS₂ the intralayer distance Sn-S decrease slowly, whereas the interlayers interatomic distance S-S decreases fast and continuously. Individual distance compressibility rates $d_i = -(1/d_0)(\partial d_i/\partial P)_T$ ($i = d_{intralayer}, d_{interlayers}$) were calculated for both compounds. For SnSe₂, $d_{intralayer} = 0.0504 \text{ GPa}^{-1}$ and $d_{interlayers} = 0.0853 \text{ GPa}^{-1}$, while for SnS₂, $d_{intralayer} = 0.0232 \text{ GPa}^{-1}$ and $d_{interlayers} = 0.1524 \text{ GPa}^{-1}$. From these values, one can see that, for SnSe₂, the change in the interlayers distance Se-Se is 41 % faster than that in the intralayer distance Sn-

Se, while for SnS₂, the interlayers distance S-S changes 85 % faster than the intralayer distance Sn-S. It is evidenced above that the increase in the average PF for SnS₂ at 20 GPa and at 800 K may be associated with the decrease of the interlayers distance S-S, increasing the electrical conductivity along the *c*-axis. If we assume that this is true, for SnSe₂ at the same conditions, a reduction of half in the average PF is expected. Therefore, the figure of merit ZT for SnSe₂ can be smaller than that for SnS₂ at 20 GPa and 800 K.

V. CONCLUSIONS

This study reports the results obtained of application of an approach combining the Rietveld method and pairs distribution function analysis to study crystalline materials under high-pressure and/or temperature for trigonal SnSe₂ and SnS₂. The refined structural parameters obtained from the Rietveld refinement of the XRD patterns measured for SnSe₂ and for SnS₂ (taken from Ref. [11]) were used as input data to simulate the partial and total structure factors $S_{Sn-Sn}(K)$, $S_{Sn-Se}(K)$, $S_{Sn-S}(K)$, $S_{Se-Se}(K)$, $S_{S-S}(K)$, $S_{SnSe_2}(K)$, and $S_{SnS_2}(K)$. Fourier transformation of them permitted to obtain the partial and total pairs distribution functions $G_{Sn-Sn}(R)$, $G_{Sn-Se}(R)$, $G_{Sn-S}(R)$, $G_{Se-Se}(R)$, $G_{S-S}(R)$, $G_{SnSe_2}(R)$, and $G_{SnS_2}(R)$. Using the structural data obtained from the Rietveld refinement, the pressure dependence of the smallest angle Sn-X (X=Se,S)-Sn, intralayer distance Sn-X (X=Se,S), and interlayers distance X-X (X=Se,S) were studied. For both the trigonal SnSe₂ and SnS₂ structures is shown that the interlayers distances change faster than the intralayer distances. Using calculated data for the thermoelectric power (*S*), electrical conductivity (σ), thermoelectric power factor (PF) along *a*- and *c*-axes, and average PF for SnS₂, and the interlayers and intralayer distances obtained from the refined structural data for SnS₂, it was evidenced that the enhancement of average

power factor observed at 20 GPa and 800 K may be associated with the fast decrease of the interlayers distance X-X (X=Se,S).

ACKNOWLEDGMENTS

One of the authors (Z. V. Borges) was financially supported by a scholarship from CNPq.

REFERENCES

- [1] H. M. Rietveld, *J. Appl. Crystallogr.* **2** (1969) 65.
- [2] T. E. Faber and J. M. Ziman, *Philos. Mag.* **11** (1965) 153.
- [3] C. N. J. Wagner, *Liquid Metals* (S. Z. Beer, Marcel Dekker, New York, 1972).
- [4] J. C. de Lima, D. Raoux, J. M. Tonnerre, D. Udron, K. D. Machado, T. A. Grandi, C. E. M. de Campos, T. I. Morrison, *Phys. Rev. B* **67** (2003) 094210.
- [5] J. C. de Lima, Z. V. Borges, C. M. Poffo, S. M. Souza, D. M. Trichês, R.S. de Biasi, Cornell University Library, arXiv.org>cond-mat>arXiv:1802.04648.
- [6] A. S. Ferreira, P. B. Prates, C. M. Poffo, J. C. de Lima, R. S. de Biasi, *Materials Research*, DOI: <http://dx.doi.org/10.1590/1980-5373-MR-2016-0788>.
- [7] P. R. Rovani, A. S. Ferreira, A. S. Pereira, J. C. de Lima, *J. Appl. Phys.* **122** (2017) 035904.
- [8] A. Larson and R. von Dreele, *GSAS Manual*, Rep. LAUR 86-748, Los Alamos National Laboratory, Los Alamos, 1988.
- [9] X. Lü, Q. Hu, W. Yang, L. Bai, H. Sheng, L. Wang, F. Huang, J. Wen, D. J. Miller, Y. Zhao, *J. Am. Chem. Soc.*, [dx.doi.org/10.1021/ja407108u](https://doi.org/10.1021/ja407108u).
- [10] H. K. Mao, B. Chen, J. Chen, K. Li, J. F. Lin, W. Yang, H. Zheng, *Matter and Radiation at Extremes* **1** (2016) 59.

- [11] M. Ø. Filsø, E. Eikeland, J. Zhang, S. R. Madsen, B. B. Iversen, Dalton Transactions, DOI: 10.1039/c5dt04532k.
- [12] Y. Javed, M. A. Rafiq, N. Ahmed, RSC Adv. 7 (2017) 38834.
- [13] Z. V. Borges, C. M. Poffo, J. C. de Lima, S. M. de Souza, D. M. Trichês, T. P. O. Nogueira, L. Manzato and R. S. de Biasi, Mater. Chem. Phys. **169**, 47 (2016).
- [14] H. K. Mao, J. Xu and P. M. Bell, J. Geophys. Res. **91**, 4673 (1986).
- [15] A. P. Hammersley, S. O. Svensson, M. Hanfland, A. N. Fitch and D. Hausermann, High Press. Res. **14**, 235 (1996).
- [16] Inorganic Crystal Structure Database (ICSD), Gmelin - Institute Fur Anorganische Chemie and Fachinformationszentrum FIZ, 1995.
- [17] Crystal Office 98 Software, Atomic Softek, Hamilton, Ontario, Canada.

TABLES

TABLE 1: Lattice parameters, volume, z atomic coordinate of site $2d$, reduced χ^2 and R factors obtained from the Rietveld refinements for the SnSe_2 trigonal phase for the applied pressures.

| P (GPa) | a (Å) | c (Å) | V (Å ³) | z (Se) | R_{wp} (%) | R_p (%) | χ^2 |
|----------------------------|----------|---------|-----------------------|----------|--------------|-----------|----------|
| 0.0(1) | 3.811(1) | 6.13(7) | 77.19(1) | 0.25 | 5.81 | 4.7 | 6.895 |
| 2.8(1) | 3.757(2) | 5.86(4) | 71.69(3) | 0.250(7) | 3.44 | 2.43 | 0.1086 |
| 3.6(1) | 3.745(1) | 5.81(3) | 70.61(6) | 0.251(1) | 3.37 | 2.66 | 0.09543 |
| 4.1(1) | 3.739(5) | 5.77(7) | 69.96(3) | 0.251(2) | 3.57 | 2.76 | 0.1009 |
| 5.1(1) | 3.723(6) | 5.71(9) | 68.67(4) | 0.251(5) | 4.28 | 3.48 | 0.1091 |
| 5.6(1) | 3.719(4) | 5.70(4) | 68.33(2) | 0.251(7) | 4.33 | 3.51 | 0.1095 |
| 6.0(1) | 3.714(6) | 5.68(7) | 67.95(7) | 0.251(8) | 3.28 | 2.67 | 0.09661 |
| 6.5(1) | 3.707(9) | 5.66(3) | 67.43(1) | 0.251(8) | 2.26 | 1.78 | 0.0597 |
| 7.0(1) | 3.702(9) | 5.65(1) | 67.09(7) | 0.252(1) | 3.47 | 2.74 | 0.09212 |
| 9.0(1) | 3.680(6) | 5.57(4) | 65.39(9) | 0.252(3) | 1.50 | 1.13 | 0.02936 |
| 9.4(1) | 3.676(2) | 5.56(2) | 65.09(3) | 0.252(4) | 0.97 | 0.74 | 0.0185 |
| 10.0(1) | 3.671(1) | 5.55(2) | 64.79(4) | 0.252(5) | 1.84 | 1.13 | 0.02604 |
| 10.5(1) | 3.667(6) | 5.53(1) | 64.43(6) | 0.252(0) | 0.67 | 0.5 | 0.01345 |
| 13.3(1) | 3.640(9) | 5.46(1) | 62.69(7) | 0.251(9) | 0.60 | 0.43 | 0.01293 |
| 14.3(1) | 3.630(3) | 5.43(9) | 62.08(8) | 0.251(9) | 1.68 | 1.31 | 0.03338 |
| 16.2(1) | 3.613(6) | 5.38(4) | 60.88(5) | 0.253(1) | 2.01 | 1.56 | 0.0481 |
| 18.4(1) | 3.600(2) | 5.35(4) | 60.10(1) | 0.253(4) | 1.53 | 1.22 | 0.03715 |
| 23.3(1) | 3.565(3) | 5.26(1) | 57.90(7) | 0.255(9) | 2.47 | 1.83 | 0.08125 |
| 25.8(1) | 3.542(1) | 5.23(1) | 56.84(3) | 0.255(9) | 2.74 | 2.08 | 0.09246 |
| Decompression (5.4 GPa) | 3.738(3) | 5.65(6) | 68.41(4) | 0.254(7) | 1.27 | 0.94 | 0.02951 |

Table 2: Structural data as a function of pressure for trigonal SnS_2 taken from Filso *et al.* [11]

Table 1 Selected crystal structure data at the 14 different pressure conditions explored. The refined space group was $P\bar{3}m1$ for the entire pressure range

| p (GPa) | a (Å) | c (Å) | V (Å ³) | z (S) | $d(\text{Sn-S})$ (Å) | $d(\text{S}\cdots\text{S})$ (Å) | $\angle(\text{Sn-S-S})$ (°) |
|-----------|-----------|------------|-----------------------|------------|----------------------|---------------------------------|-----------------------------|
| 0.0001 | 3.6456(4) | 5.8934(11) | 67.83(2) | 0.2473(3) | 2.5601(11) | 3.647(3) | 90.80(7) |
| 0.664(9) | 3.6390(3) | 5.7853(19) | 66.35(2) | 0.2513(15) | 2.555(5) | 3.563(10) | 90.82(16) |
| 1.109(11) | 3.6339(2) | 5.7322(17) | 65.56(2) | 0.2544(16) | 2.555(6) | 3.511(11) | 90.65(18) |
| 1.991(16) | 3.6215(3) | 5.650(3) | 64.18(3) | 0.2565(14) | 2.544(5) | 3.456(9) | 90.76(17) |
| 3.40(3) | 3.6067(3) | 5.544(2) | 62.46(3) | 0.2631(14) | 2.542(5) | 3.352(9) | 90.36(15) |
| 4.22(3) | 3.5983(4) | 5.494(3) | 61.61(3) | 0.2639(10) | 2.533(4) | 3.324(7) | 90.50(13) |
| 6.29(5) | 3.5766(4) | 5.393(3) | 59.74(3) | 0.2701(13) | 2.527(5) | 3.227(8) | 90.09(14) |
| 8.08(6) | 3.5605(4) | 5.317(3) | 58.37(3) | 0.2729(16) | 2.516(5) | 3.171(10) | 90.07(16) |
| 9.78(8) | 3.5455(3) | 5.257(3) | 57.23(3) | 0.2738(18) | 2.502(6) | 3.138(11) | 90.21(17) |
| 11.88(9) | 3.5388(3) | 5.157(2) | 56.13(3) | 0.2775(15) | 2.497(5) | 3.079(9) | 90.23(15) |
| 13.68(19) | 3.5362(4) | 5.100(3) | 55.23(3) | 0.2836(15) | 2.502(5) | 3.007(8) | 89.93(15) |
| 14.8(2) | 3.5343(4) | 5.068(3) | 54.82(3) | 0.2839(12) | 2.497(4) | 2.994(7) | 90.11(13) |
| 16.8(4) | 3.5272(4) | 5.026(3) | 54.16(3) | 0.2859(17) | 2.492(5) | 2.963(9) | 90.08(16) |
| 20(1) | 3.5074(7) | 4.978(4) | 53.05(5) | 0.2879(19) | 2.481(6) | 2.926(10) | 89.97(17) |

FIGURES

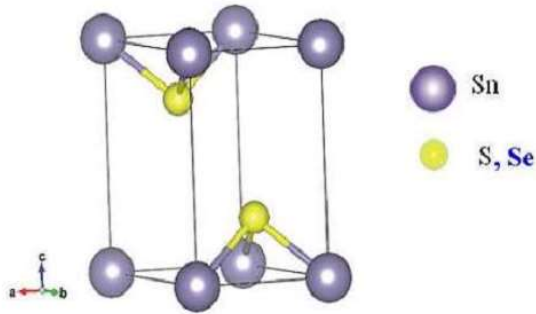


Figure 1: Conventional unit cell of trigonal SnSe_2 and SnS_2 .

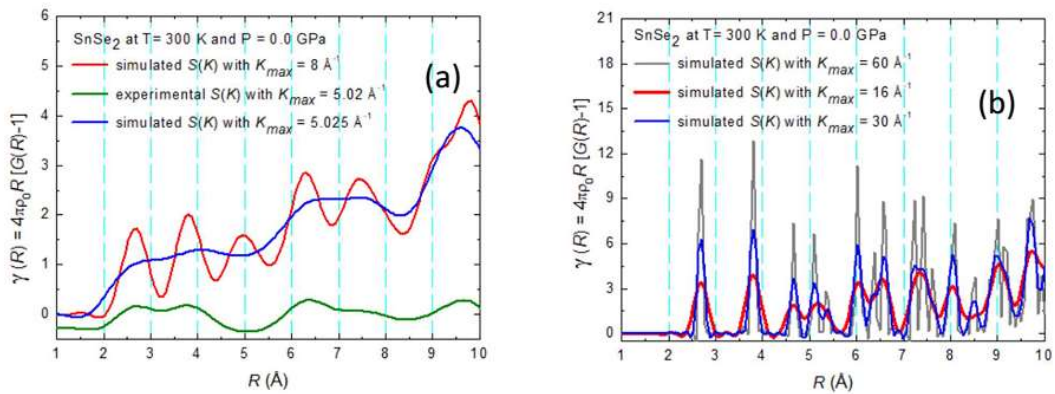
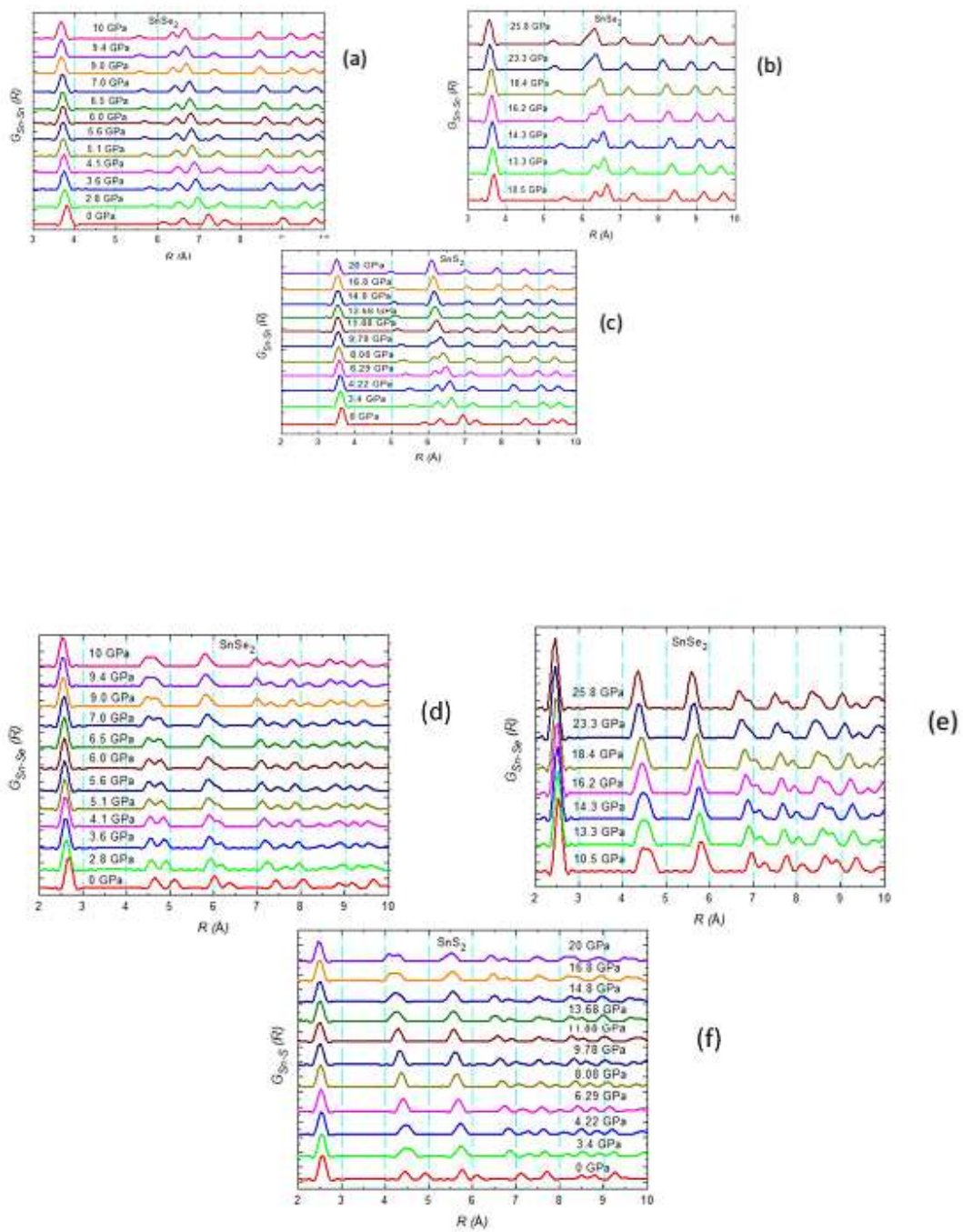
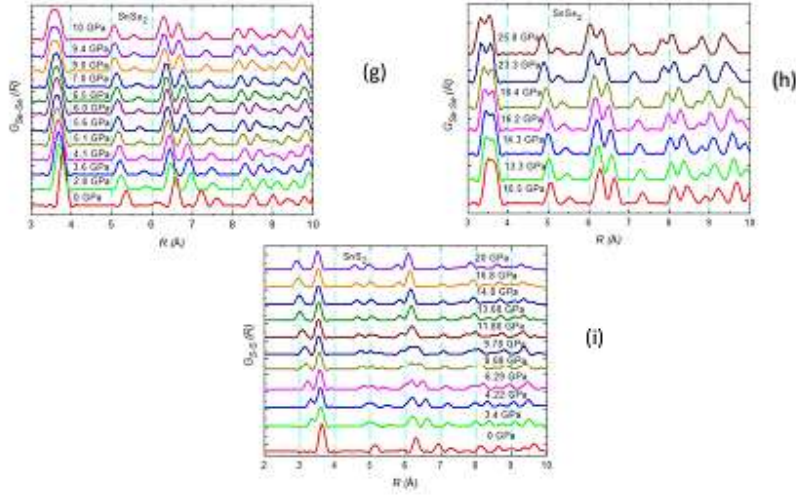


Figure 2: Experimental pair distribution function $G(R)$ of trigonal SnSe_2 at atmospheric pressure and simulated with different values of the transferred momentum K vector.





Figures 3(a)-(c), (d)-(f) and (g)-(i): Pressure dependence of the simulated $G_{Sn-Sn}(R)$, $G_{Sn-Se}(R)$, $G_{Sn-S}(R)$, $G_{Se-Se}(R)$, and $G_{S-S}(R)$ functions for trigonal $SnSe_2$ and SnS_2 , with $K_{max} = 30 \text{ \AA}^{-1}$.

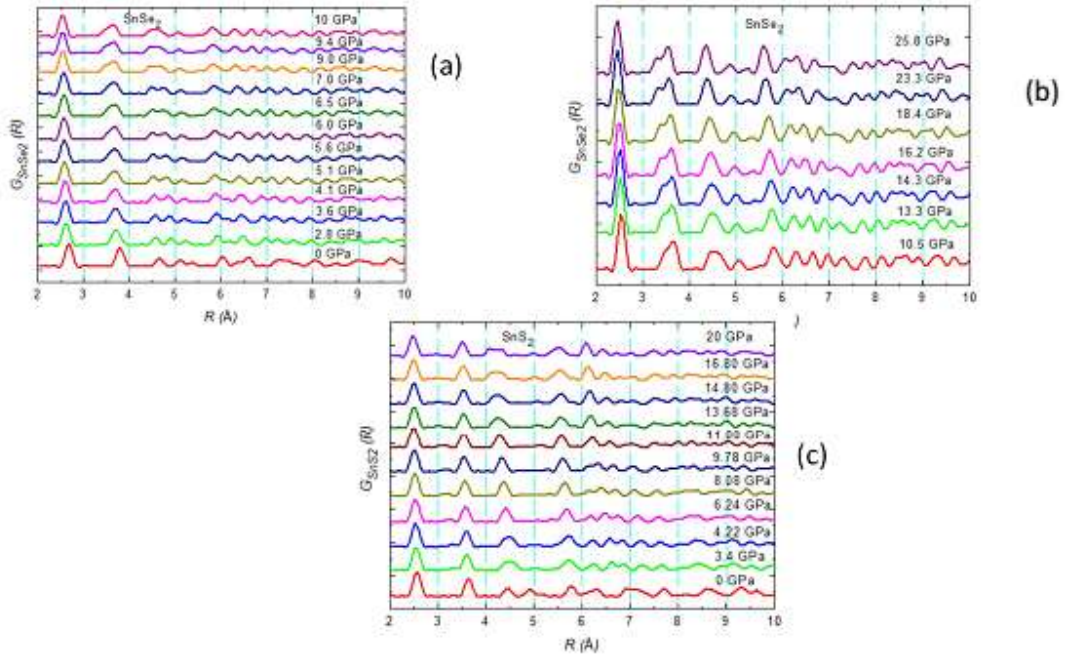


Figure 4(a)-(c): Pressure dependence of the simulated G_{SnSe_2} and $G_{SnS_2}(R)$ functions for trigonal $SnSe_2$ and SnS_2 , with $K_{max} = 30 \text{ \AA}^{-1}$.

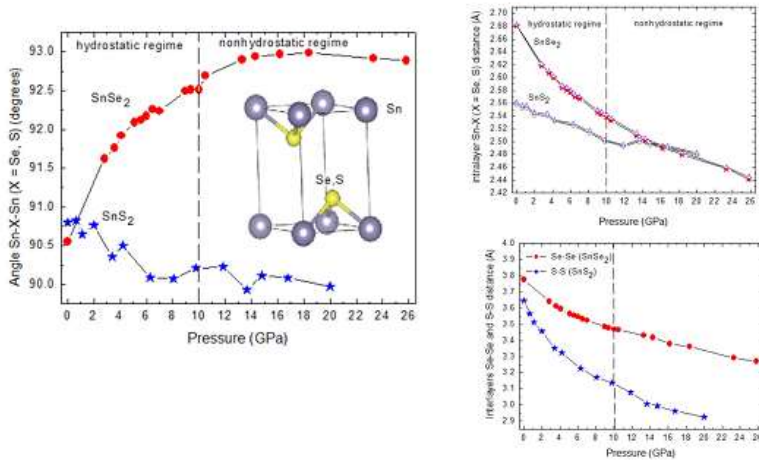


Figure 5: Pressure dependence of angle Sn-X (X=Se,S)-Sn and of intralayer distances Sn-X (X=Se,S) and interlayers distances X-X (X=Se,S).

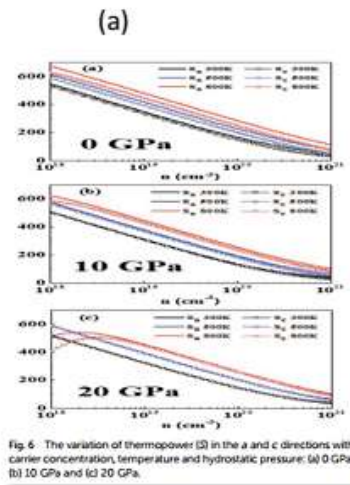


Fig. 6 The variation of thermopower (S) in the a and c directions with carrier concentration, temperature and hydrostatic pressure: (a) 0 GPa, (b) 10 GPa and (c) 20 GPa.

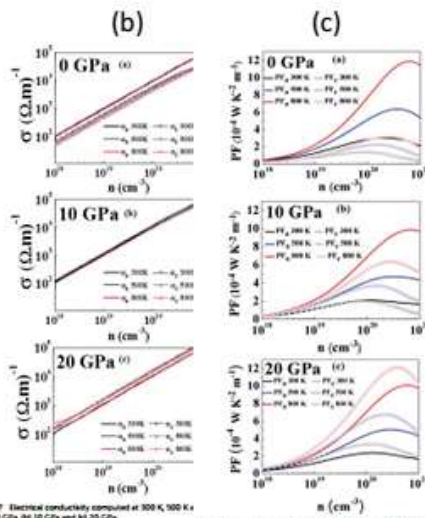


Fig. 7 Electrical conductivity computed at 300 K, 500 K and 800 K at (a) 0 GPa, (b) 10 GPa and (c) 20 GPa.

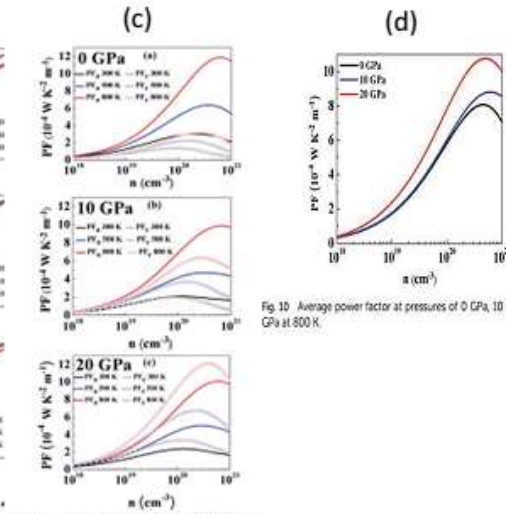


Fig. 8 Power factor at 300 K, 500 K and 800 K at (a) 0 GPa, (b) 10 GPa and (c) 20 GPa.

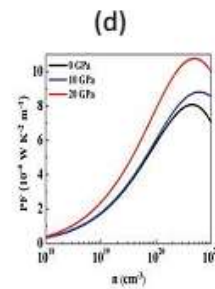


Fig. 9 Average power factor at pressures of 0 GPa, 10 GPa and 20 GPa at 800 K.

Figure 6(a)-(d): Pressure dependence of the thermoelectric power (S), electrical conductivity (σ), power factor (PF), and average power factor at atmospheric pressure, 10 GPa, and 20 GPa at temperatures 300 K, 500 K and 800 K, taken from Ref. [12].